RESEARCH ARTICLE
SOLID EARTH: TECTONOPHYSICS

Earth and Planetary Physics
9: 1037–1047, 2025
doi: 10.26464/epp2025079

Subduction plate age as a control on elastic upper-plate thickness in Cascadia: Insights from interseismic GNSS observations and implications

ShaoYang Li[1*], and Ling Chen[1,2]

[1]State Key Laboratory of Lithospheric and Environmental Coevolution, Institute of Geology and Geophysics, Chinese Academy of Sciences, Beijing 100029, China;

[2]College of Earth and Planetary Sciences, University of Chinese Academy of Sciences, Beijing 100049, China

Key Points:

- Forward viscoelastic models show a strong trade-off between locking depth and elastic upper-plate thickness (H_c), requiring additional constraints.
- Elastic upper-plate thickness (H_c) increases systematically northward from ~20 to 30 km, correlating with the age of the oceanic plate and, consequently, its cooling along the Cascadia forearc.
- Lateral H_c variations alter earthquake-cycle deformation patterns and should be included in seismic hazard assessments.

Citation: Li, S. Y., and Chen, L. (2025). Subduction plate age as a control on elastic upper-plate thickness in Cascadia: Insights from interseismic GNSS observations and implications. *Earth Planet. Phys.*, *9*(5), 1037–1047. http://doi.org/10.26464/epp2025079

Abstract: Understanding the viscoelastic structure of subduction zones is essential for assessing seismic hazards and understanding subduction-zone dynamics. However, the influence of lateral variations in elastic upper-plate thickness (H_c) remains poorly constrained and is often overlooked. In this study, we use two-dimensional forward viscoelastic earthquake-cycle models to fit both horizontal and vertical Global Navigation Satellite System (GNSS) observations. We identify a clear trade-off between locking depth (D) and H_c in both components. To resolve this ambiguity, we incorporate constraints from thermal models and tremor distributions along the Cascadia Subduction Zone. As a novel result extending beyond previous kinematic models, our results reveal a systematic northward increase in H_c from ~20 km to ~30 km. This trend correlates with increasing oceanic plate age and likely reflects variations in the subaccretion and wedge-cooling processes along the trench-parallel direction. In contrast, D remains relatively uniform at ~10 km, consistent with previous findings. These results demonstrate the robustness of our approach for simultaneously constraining H_c and D, and they suggest it may be applied to other subduction zones. Lateral variations in H_c significantly affect crust deformation and should not be ignored in earthquake-cycle models. Accounting for these heterogeneities improves estimates of H_c and D and enhances our understanding of megathrust locking, seismic hazard potential, and the physical conditions controlling episodic tremor and slip events.

Keywords: elastic upper-plate thickness; megathrust locking depth; Cascadia; episodic tremor and slip; finite-element models; Global Navigation Satellite System (GNSS)

1. Introduction

The outer layer of the viscoelastic Earth is characterized by a colder, rigid lithosphere flowing over the hotter, ductile asthenosphere (Bott and Dean, 1973; Cohen, 1999; Wang KL et al., 2012). Between these two layers, the lithosphere–asthenosphere boundary represents a mechanical transition from elastic to viscoelastic behavior and has been extensively characterized using thermal, seismological, geodetic, and experimental observations (McKenzie, 1967; Chen L et al., 2006; Bürgmann and Dresen, 2008; Kawakatsu et al., 2009; Hu Y et al., 2016; Wang X et al., 2024). This boundary is considered a critically important region where vigorous physical and chemical processes occur at depth over various time scales (Hirth and Kohlstedt, 2004; Bürgmann and Dresen, 2008; Burov, 2011). On geologic time scales (millions of years), it is thought to influence the efficiency of plate tectonics and planetary habitability (Fischer et al., 2010; Rychert et al., 2020; Lu et al., 2021). On shorter earthquake-cycle time scales (hundreds of years), this transition zone also plays a key role in earthquake dynamics, including the nucleation and termination of fast earthquakes (Chen WP and Molnar, 1983; Hyndman et al., 1997; Bilham et al., 2017) and the generation of slow earthquakes (collectively referred to hereafter as tremors, low-frequency earthquakes, very low-frequency earthquakes, and slow slip events; Dragert et al., 2001; Obara, 2002; Rogers and Dragert, 2003; Shelly et al., 2007). Therefore, quantifying the lithosphere–asthenosphere system in

Correspondence to: S. Y. Li, shaoyangli@mail.iggcas.ac.cn
Received 09 APR 2025; Accepted 18 JUN 2025.
First Published online 21 JUL 2025.

terms of lithosphere thickness and asthenosphere rheology through geophysical measurements is a critical priority in solid Earth studies.

Geodetically, the lithosphere–asthenosphere system can typically be probed through postseismic deformation induced by coseismic stress perturbations from large subduction earthquakes (e.g., Nur and Mavko, 1974; Pollitz et al., 2008; Suito and Freymueller, 2009; Sun THZ et al., 2014; Hu Y et al., 2016; Li SY et al., 2018a; Weiss et al., 2019). Modeling postseismic deformation has provided fundamental insights into asthenosphere rheology over the past few decades, including the immediate excitation of viscoelastic relaxation following major earthquakes (Sun THZ et al., 2014; Sobolev and Muldashev, 2017), spatial heterogeneity in mantle viscosity (Wiseman et al., 2015; Muto et al., 2016; Freed et al., 2017), its temporal evolution (Li SY et al., 2018a), and the relative contributions of afterslip and viscoelastic relaxation to surface deformation (Qiu Q et al., 2018; Muto et al., 2019; Fukuda and Johnson, 2021). All point to the importance of the viscoelastic response of the Earth. Despite these advances, interseismic deformation—typically attributed to megathrust interface locking—is widely modeled using purely elastic Earth theory (e.g., Okada, 1992; McCaffrey, 2002; Meade and Loveless, 2009). Given the viscoelastic nature of the Earth, the tectonic loading process (e.g., megathrust locking) is also expected to induce observable viscoelastic responses in the asthenosphere, forming longer wavelength horizontal interseismic deformation than the conventional elastic models (Wang KL et al., 2001; Trubienko et al., 2013; Li SY et al., 2015, 2020; Li SY and Chen L, 2023), similar to those observed during tectonic unloading processes (e.g., viscoelastic relaxation driven by coseismic rupture and glacial isostatic adjustment). Thus, observations of interseismic deformation also hold the potential to constrain the viscoelastic behavior of the subduction system in detail (Li SY et al., 2015; Itoh et al., 2019; Diao FQ et al., 2022; Li SY and Chen L, 2024a).

The Cascadia Subduction Zone, where the Juan de Fuca Plate subducts beneath the North American Plate (DeMets et al., 2010; Figure 1), is a well-known seismic gap that has produced major megathrust earthquakes, with the most recent *M*9 event occurring in AD 1700 (Atwater, 1987; Satake et al., 2003; Goldfinger et al., 2017). The seismically quiescent period of the margin (Toda and Stein, 2022) makes geodetic observations particularly critical for studying its geodynamics. Early elastic modeling of contemporary geodetic data (e.g., Figure 1) conclusively identified the interseismic locking of the megathrust (Khazaradze et al., 1999; Wang KL et al., 2003; McCaffrey et al., 2013; Schmalzle et al., 2014). More recent geodetic modeling has revealed the viscoelastic component of the deformation field (e.g., Wang KL et al., 2012; Pollitz and Evans, 2017; Li SY et al., 2018b; Pollitz, 2025), which aligns with a viscoelastic earthquake-cycle framework (Wang KL et al., 2012; Li SY and Chen L, 2023). These locking models generally show a shallow locking depth and a deeper band of slow earthquakes occurring within the brittle–ductile transition zone, with a gap between them in this warm subduction zone (e.g., Hyndman, 2013; Audet and Kim, 2016; Gao X and Wang KL, 2017; Li SY et al., 2018b).

Previous modeling of interseismic deformation in Cascadia—and in many other subduction zones—has primarily focused on resolving the spatial distribution of megathrust locking while often treating the viscoelastic structure as a simplified, predefined parameter. A key assumption in these models is a laterally uniform elastic upper-plate thickness (i.e., continental lithosphere) along the trench-parallel direction, despite substantial geophysical

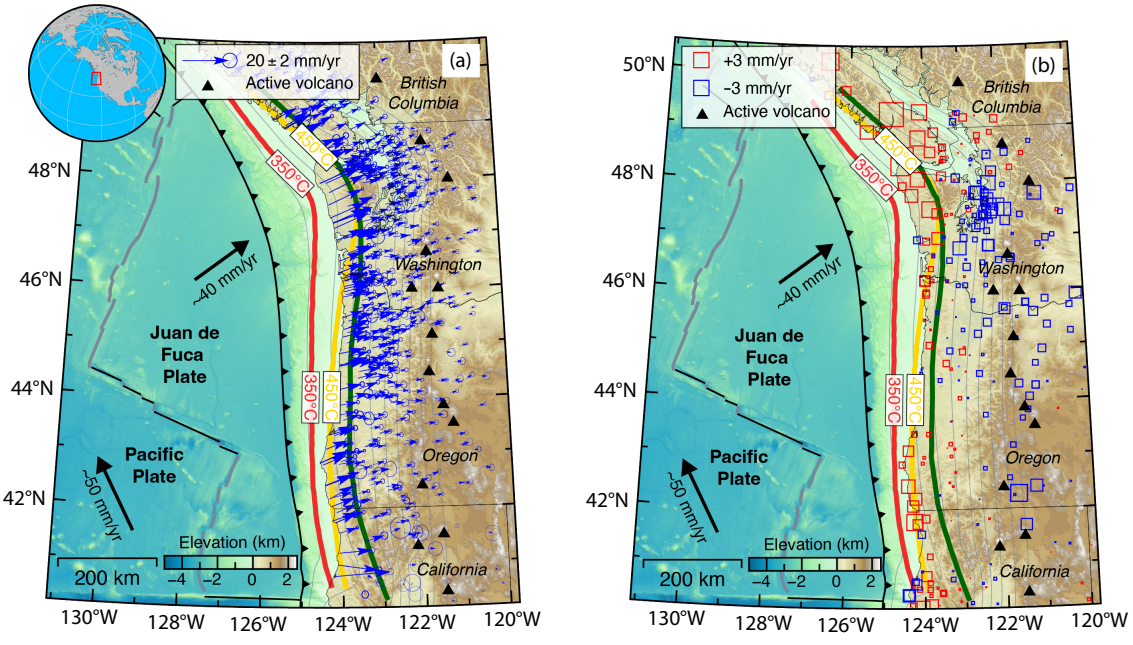

Figure 1. Tectonic settings and contemporary deformation of the Cascadia Subduction Zone. (a) Horizontal interseismic velocities processed by McCaffrey et al. (2013) and Li SY et al. (2018b). Inset shows the global location of the study area (red trapezoid). (b) Vertical interseismic velocities processed by Michel et al. (2019). The thick red and yellow lines are downdip depths of fully locked and transition zones, respectively, determined from the thermal model (Hyndman and Wang K, 1995). The thick green line is the updip depth of the tremor zone from Wirth and Frankel (2019). The thin gray contours are the megathrust depth at 10-km intervals.

evidence for lateral heterogeneities in Cascadia (e.g., Blakely et al., 2005; Porritt et al., 2011; Littel et al., 2018; Bodmer et al., 2020; Delph et al., 2021; Egbert et al., 2022; Yu CH et al., 2022; Cao ZB and Liu LJ, 2024). Consequently, the potential influence of upper-plate elastic thickness on locking estimates remains poorly understood. Moreover, many of these studies rely on inverse methods incorporating regularization techniques such as smoothing, which can obscure the transitions between locked, creeping, and slow-slip regions (Li SY and Chen L, 2024b; Sato et al., 2024; Sherrill et al., 2024). Such smoothing may hinder accurate comparisons between locking depths and the assumed elastic plate thickness, potentially leading to misinterpretation of physical processes underlying episodic tremor and slip (ETS) in Cascadia and elsewhere. To address these limitations, we adopt a forward modeling approach that simulates surface deformation to fit observed interseismic Global Navigation Satellite System (GNSS) velocities (Figure 1), allowing us to directly constrain the viscoelastic structure of the overriding plate. To refine model parameters and reduce nonuniqueness, we incorporate additional prior constraints from independent geophysical observations, particularly thermal modeling (Figure 1), following the similar modeling strategy of Li SY and Chen L (2024b). The lateral variations obtained in elastic upper-plate thickness are found to correlate well with the oceanic plate age (Wells et al., 1998; Wilson, 2002) and are then interpreted in the context of earthquake-cycle deformation and ETS processes, offering new insights into the subduction-zone dynamics in Cascadia.

2. Data and Method

2.1 Decadal GNSS Velocities

Following Li SY et al. (2018b) and Li SY and Chen L (2024b), we utilize decade-scale horizontal velocities from McCaffrey et al. (2013) and vertical velocities from Michel et al. (2019). These velocities (Figure 2) are derived from both continuous and campaign GNSS sites, with the effects of episodic slow slip averaged out. The vertical deformation rates have not been corrected for postglacial rebound (e.g., Peltier et al., 2015), whereas the horizontal velocities are defined relative to a stable North America reference frame, enabling direct comparison with finite-element modeling results that use fixed far-field boundaries. Long-term geological deformation—assumed to be independent of megathrust earthquake cycles—has been removed as "block motion" following Schmalzle et al. (2014), and alternative corrections have been shown to produce no significant differences in the deformation pattern (Li SY et al., 2018b). The corrected horizontal velocities are attributed entirely to megathrust locking and creep. However, because the magnitude of the correction generally increases from north to south (Li SY et al., 2018b) and because of postseismic deformation from the triple junction earthquakes, we expect that the uncertainties in the modeled fault kinematics also increase toward the southern end of the study area.

Without advanced modeling, the GNSS-derived horizontal and vertical velocities already reveal the typical interseismic deformation patterns associated with a locked megathrust and coherent deformation along the Cascadia trench (Figure 2). Specifically, the horizontal velocities (0–25 mm/yr) display a more than 600-km long-wavelength landward decrease across the forearc, arc, and backarc regions (Figure 2a), which is consistent with interseismic strain accumulation predicted by a viscoelastic Earth model (Li SY et al., 2018b). In contrast, the vertical velocities, with much lower magnitudes ranging from −4 to 4 mm/yr, exhibit a distinct subsidence–uplift–subsidence pattern away from the trench (Figure

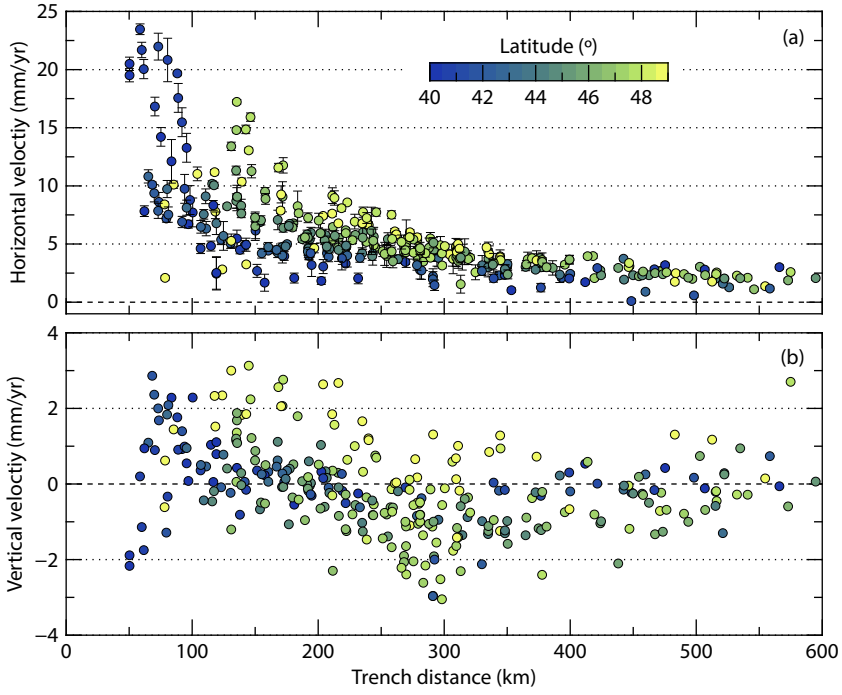

Figure 2. Lateral variations of GNSS velocities (color-coded as the site latitudes) as a function of trench distance in the (a) horizontal and (b) vertical directions.

2b) that aligns with predictions from a viscoelastic earthquake-cycle model (Li SY and Chen L, 2024a). Notably, the subsidence signal related to the viscoelastic mantle flow in the backarc region (250–500 km trench distance) is particularly pronounced. Both components also highlight lateral variations along the trench-parallel direction, likely reflecting differences in plate coupling, megathrust geometry, the structure of the viscoelastic lithosphere –asthenosphere system, or their combination. For instance, compared with northern velocities, southern velocities show both a relatively shorter horizontal wavelength and lower vertical magnitudes in the backarc region, indicating a less viscous deformation pattern. This correlation between horizontal strain gradients and vertical subsidence rates, coupled with systematic along-strike heterogeneity, underscores the value of GNSS observations in constraining the deformation dynamics of Cascadia.

2.2 Finite-Element Modeling

We construct two-dimensional (2D) finite-element models using the open-source software *PyLith* (Aagaard et al., 2013) and perform forward viscoelastic earthquake-cycle simulations to explain both horizontal and vertical GNSS velocities. Following Li SY et al. (2018b) and Li SY and Chen L (2024b), our model consists of four domains: the oceanic and continental plates, and the oceanic and continental mantle (Figure 3a). This setup captures the first-order influence of the subducting slab on viscous mantle flow—where the slab acts as an impermeable barrier to mantle flow—during both the postseismic and interseismic phases (e.g., Pollitz et al., 2008; Li SY and Chen L, 2022). To compare GNSS data within the relatively far reference frame while minimizing boundary effects, we define our model domain as 3000 km in width and 500 km in depth (Figure 3b). Continental observations are considered minimally influenced by the oceanic plate, which is therefore modeled with a uniform thickness of 30 km for simplicity (Wang KL et al., 2012). Given the importance of curved slab and megathrust geometry in determining fault kinematics (Moreno et al., 2009), we incorporate these features (Figure 3b) based on a three-dimensional (3D) geometric model (e.g., McCrory et al., 2012; Gao DW et al., 2017; Li SY et al., 2018b). Following Wang KL et al. (2012) and Li SY et al. (2018b), we assume Maxwell viscosities of 10^{19} Pa s for the continental mantle and 10^{20} Pa s for the oceanic mantle. In a steady-state subduction system, varying these viscosities does not affect the predicted surface displacement velocities (Figure S1 of Li SY et al., 2018b) and hence the obtained kinematic parameters of the model. The rigidity values for the elastic plates and mantle are set to 48 GPa and 64 GPa, respectively, whereas a Poisson's ratio of 0.25 is applied throughout the model domain. Displacements perpendicular to the lateral and bottom boundaries of the model are fixed to zero, whereas displacements parallel to these boundaries remain unconstrained. The top boundary is set as a free surface.

In this study, we introduce two key free parameters to characterize deformation rates: (1) the downdip depth D of full locking (i.e., locking degree = 1) from the trench and (2) the elastic upper-plate thickness H_c (Figure 3a). A fully locked state extending to the trench is supported by the thermal structure of the warm subduction zone and the paucity of seismicity along the entire margin (Wang KL and Tréhu, 2016). The transition zone downdip of the fully locked segment is assumed to be 10 km thick, with a nonlinear decrease in locking degree to zero, following the kinematic framework of Wang KL et al. (2003). At greater depths, an intervening gap in the subduction fault, located updip of the ETS zone (Figure 3a), has been documented in Cascadia through multiple lines of evidence (Hyndman, 2013). This separation is proposed to be mechanically controlled by the interplay of temperature and high fluid pressure (Gao X and Wang KL, 2017).

Megathrust locking is modeled by kinematically prescribing a back-slip rate distribution (Savage, 1983), calculated as the product of the locking ratio distribution and the profile-parallel convergence rate (~30–40 mm/yr; DeMets et al., 2010). For simplicity, we

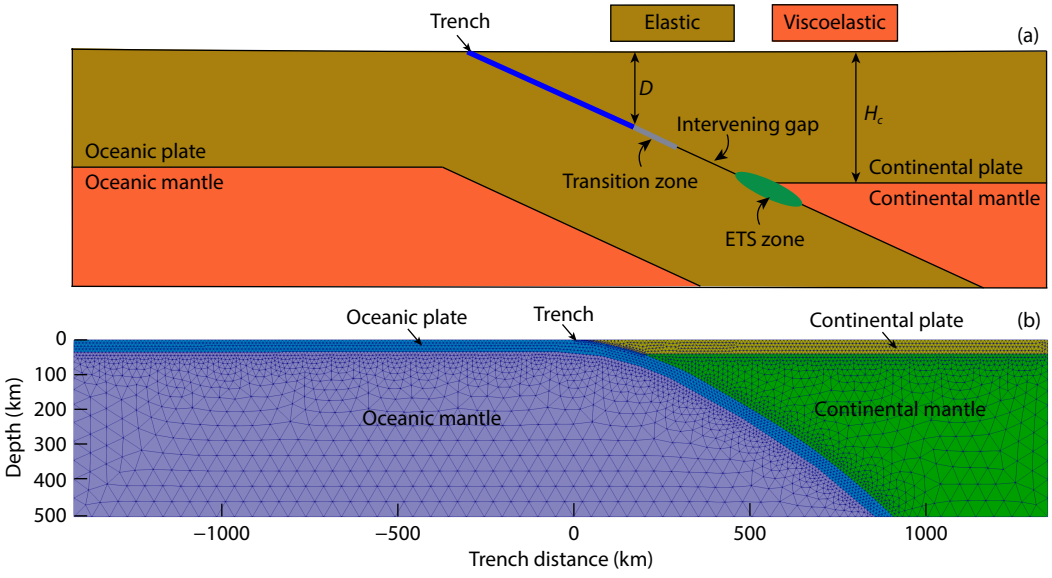

Figure 3. Model setups and geometry. (a) Illustration of the two explored free parameters (i.e., H_c and D) of the modeled Cascadia Subduction Zone. The concepts of intervening gap and ETS zone are proposed by Hyndman (2013) and Rogers and Dragert (2003), respectively. (b) An example of a finite-element model mesh aligned along the 46° latitude line.

assume an earthquake recurrence interval of 300 yr, based on the averaged interval from paleo-earthquake records (Goldfinger et al., 2017) and the rough elapsed time of the last megathrust earthquake in AD 1700 (Satake et al., 2003), and that the slip deficit accumulated during each cycle is fully released in coseismic rupture events (Li SY et al., 2020; Li SY and Chen L, 2023). This recurrence time is similar to the elapsed time since the last earthquake at the time GNSS data were collected mainly during the first decade of the 21st century (McCaffrey et al., 2013), and varying this time does not change the predicted displacement velocities because of the steady state of the subduction system (Figure S1 of Li SY et al., 2018b). We run our viscoelastic models over 10 earthquake cycles to reach a steady state (e.g., Hetland and Hager, 2006) and extract the 5-yr-averaged velocities before the next earthquake for comparison with GNSS data, following the approach of Li SY et al. (2020). The GNSS velocities within 80-km-wide, margin-normal swath profiles are used to compare with predictions from the models with the corresponding local slab geometry. The goodness-of-fit between observed and modeled horizontal and vertical velocities is evaluated using the root mean square (RMS) misfit. Varying the width of the profiles for selecting the data does not significantly change the results. To explore the first-order variations of H_c and D along the trench-parallel direction and minimize the 3D effects, we primarily analyze four 2D profiles aligned with latitude (i.e., 42°, 44°, 46°, and 48°). Profiles farther to the south (40°) and north (50°) are excluded owing to, respectively, large uncertainties (caused by block motion and postseismic deformation of nearby earthquakes) and sparse data coverage (Figure 1).

Given the inherent nonuniqueness of geodetic data in constraining a kinematic model, we further refine the parameter space of H_c and D using prior constraints from thermal modeling (Hyndman and Wang K, 1995), the depth of the ETS zone (30–40 km; Rogers and Dragert, 2003; Gao X and Wang KL, 2017), and the updip extent of the tremor zone (Wirth and Frankel, 2019). The uncertainty in temperature-based locking depth estimates is approximately ±25 °C, with the 100 °C isotherm corresponding to depths of 10–20 km (thick yellow and red curves in Figure 1; Hyndman and Wang K, 1995). Consequently, the associated depth uncertainty is assumed to be 2.5–5 km. As shown in the following section, these constraints of D prove to be valuable in refining H_c, given the trade-off between H_c and D in our models.

3. Results and Discussion

3.1 Trade-Off Between H_c and D

The first-order controls of interseismic deformation by the locking depth of the plate interface and the Earth's viscoelasticity have been well established through both elastic and viscoelastic models (Savage, 1983; Trubienko et al., 2013; Li SY et al., 2015). In particular, for a given convergence rate, a deeper locking depth results in higher deformation rates and a broader deformation pattern. In our viscoelastic models, which account for earthquake cycles and historical earthquakes, this control of D remains valid: deeper locking leads to higher predicted horizontal velocities across the entire upper plate (Figure 4a). The impact of H_c on interseismic surface deformation can be readily analyzed using the (semi)analytical solutions of layered Earth models (e.g., Wang RJ et al., 2006; Noda et al., 2018). Our subduction models further illustrate the clear influence of H_c, with its effect varying depending on the distance from the trench (Figure 4b). For instance, when D = 10 km, the influence of H_c is most pronounced within a trench distance range of 100–400 km, whereas it is weaker both closer to and farther from the trench (Figure 4b). This result suggests that observations within this range can be used to constrain H_c. Additionally, for a given D, the effect of H_c exhibits a saturation pattern with increasing H_c. For example, when D = 10 km and H_c > 40 km, further increases in H_c do not significantly alter the predicted deformation rate curve (Figure 4b). This saturation effect indicates a potential limitation in using deformation data to constrain H_c if its value is too large.

The trade-off between H_c and D is expected, as both parameters exert a substantial influence on surface deformation (e.g., >5 mm/yr, which is much larger than GNSS observation errors; Figure 4). However, this trade-off has been underappreciated in previous studies. To further explore this relationship, we systematically vary both parameters and evaluate the horizontal GNSS data misfit across different models (Figure 5). Using the misfit curves as a criterion for assessing model performance, as is conventionally done, we find that multiple combinations of H_c and D can yield similarly low misfit values, defining preferred parameter ranges (e.g., 5 < D < 12.5 km and 10 < H_c < 50 km; Figure 5a). Conversely, certain parameter ranges are disfavored by the GNSS data; for instance, when D > 20 km, the data misfit increases substantially (Figure 5b). These findings suggest that although GNSS data can help identify plausible and implausible parameter ranges, it alone

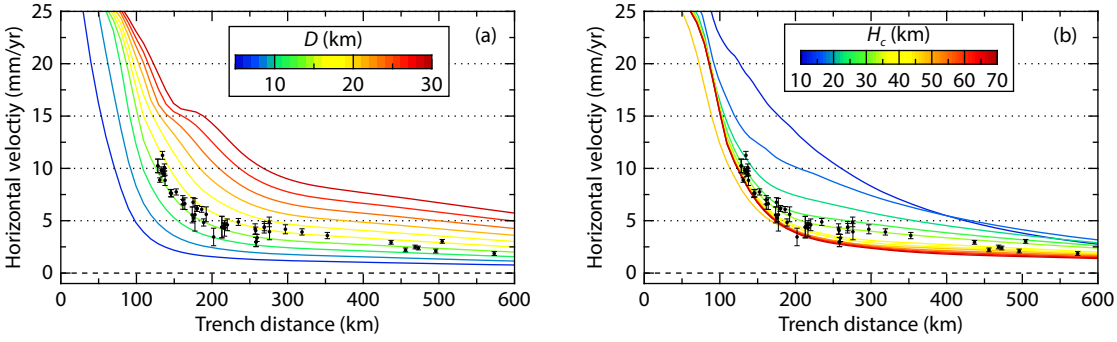

Figure 4. Impacts of (a) full locking depth (D) and (b) elastic upper-plate thickness (H_c) on the fitting of horizontal GNSS data along the latitude 46° profile. H_c of models shown in (a) and D of models shown in (b) are assumed to be 40 km and 10 km, respectively.

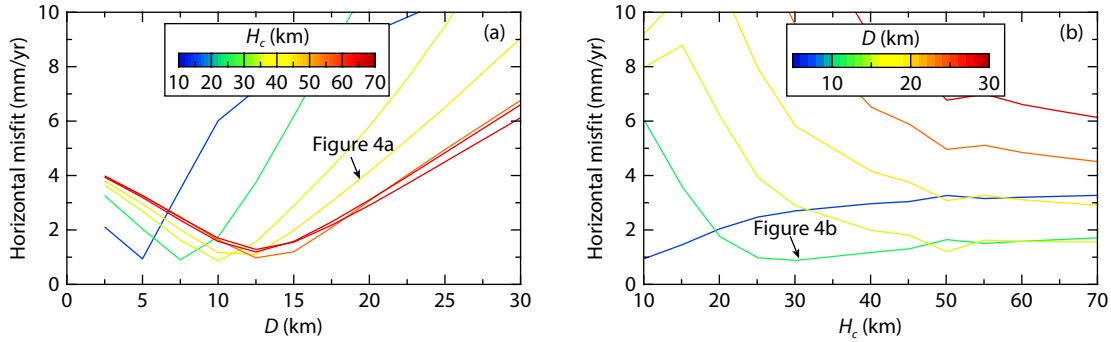

Figure 5. Trade-off between full locking depth (D) and elastic upper-plate thickness (H_c) in terms of model RMS misfit of horizontal GNSS data along the latitude 46° profile. (a) Preferred D as a function of H_c. (b) Preferred H_c as a function of D.

is insufficient to further refine the most reasonable values because of the trade-off between H_c and D. Therefore, additional constraints from multiple data sources are necessary for more robust parameter estimation. For instance, incorporating both horizontal and vertical GNSS data (Figure 6), as well as independent constraints from thermal modeling or tremor depth observations (Figure 7), can provide further refinement.

3.2 Preferred H_c from Multiple Constraints

We first examine the combined ability of horizontal and vertical GNSS data components to constrain H_c and D (Figure 6). Both components exhibit a clear trade-off between the two parameters, but in different ways. Specifically, when $H_c < 40$ km, a relatively higher H_c combined with a relatively higher D can equally explain the horizontal data (Figure 6a), whereas a relatively higher H_c combined with a relatively lower D can equally explain the vertical data (Figure 6b). For $H_c > 40$ km, neither horizontal nor vertical data can effectively constrain H_c, but both favor a similar D (~10 km for horizontal data and ~7.5 km for vertical data; Figure 6). Consistent with the findings in Section 3.1 (Figure 5), models with $D > 20$ km result in high RMS misfits for both horizontal and vertical components (Figure 6). These similarities and differences in how horizontal and vertical data constrain H_c and D suggest that both components capture the same underlying deformation process but exhibit preferences for slightly different parameter values. This distinction may be useful for refining estimates of H_c and D. Therefore, it is essential to jointly consider both horizontal and vertical data in interseismic deformation models (e.g., Li SY et al., 2020; Li SY and Chen L, 2022).

We then evaluate the total RMS misfit of horizontal and vertical data while incorporating prior constraints on D derived from thermal and seismological observations to refine estimates of H_c and D (Figure 7). Refinement can be achieved mainly because of the trade-off between H_c and D (Figure 6). In calculating the total RMS misfit, the vertical data are often weighted 3 times more than the horizontal data. However, vertical deformation in Cascadia is influenced by multiple known and unknown processes unrelated to earthquake-cycle deformation (Wang KL and Tréhu, 2016). Assigning greater weight to the vertical component complicates uncertainty quantification, whereas down-weighting it effectively discards an already subtle signal. Following Li SY et al. (2020) and to maintain methodological simplicity, we assign equal weighting to the horizontal and vertical data in this study. Jointly considering horizontal and vertical data in the total RMS misfit generally excludes models with $H_c > 40$ km (Figure 7). Additionally, prior constraints—especially the 350 °C isotherm depth (thick red line in Figure 1; Hyndman and Wang K, 1995)—help rule out models with $D < 7.5$ km (Figure 7). In contrast, the 450 °C isotherm depth and the upper limit of the tremor zone (thick green line in Figure 1; Wirth and Frankel, 2019) do not provide a stronger constraint on the upper bound of D than the GNSS data alone. This may be due to the presence of an intervening gap (Hyndman, 2013), which suggests that both the 450 °C isotherm and tremor top depth must be deeper than D. We also find that models where $D > H_c$ generally produce poor fits to the GNSS data (Figure 7), consistent with the young and warm setting of this subduction zone,

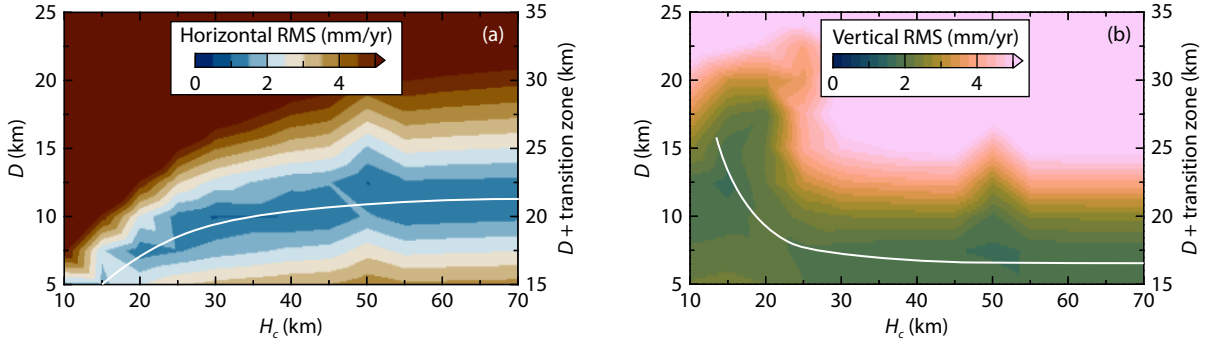

Figure 6. Performance of models with different D and H_c on fitting (a) horizontal and (b) vertical GNSS data along the latitude 46° profile, respectively. The white curves denote the inherent trade-off between H_c and D.

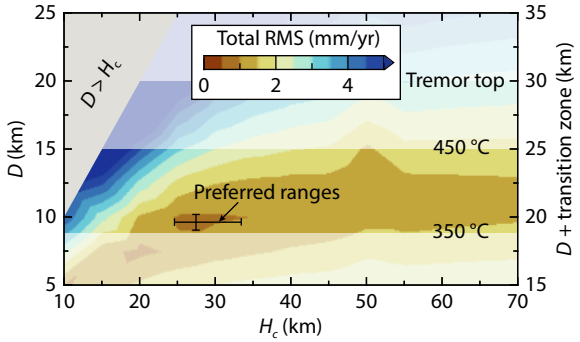

Figure 7. Determination of preferred parameter ranges for H_c and D based on the total RMS misfit of horizontal and vertical data along the 46° latitude profile, along with additional constraints at the same latitude (indicated by white and gray shading). Notably, models with D shallower than the 350 °C isotherm are excluded in this case, despite their ability to fit the GNSS data well.

where locking tends to be shallow (Oleskevich et al., 1999; Hyndman, 2013). Considering these multiple constraints, we identify relatively narrow preferred ranges for H_c and D along each profile in the trench-parallel direction (Figure 7) and synthesize lateral variations of H_c and D across the entire Cascadia Subduction Zone (Figure 8).

3.3 Lateral Variations of H_c and D

Assembling the estimated H_c values from different profiles reveals a systematic northward increase that correlates well with the increase in oceanic plate age (Figure 8a; Wells et al., 1998; Wilson, 2002). The difference in H_c between the northernmost (30 km) and southernmost (20 km) profiles reaches up to 10 km, corresponding to an approximate 5 Ma difference in subduction age beneath the forearc (Figure 8a). We propose that an old plate age cools down the forearc area (Syracuse et al., 2010; Epstein et al., 2024), resulting in an estimated growth rate of the elastic upper-plate thickness of approximately 2 km/Ma in Cascadia. Regional upper-plate geology and lithology, including the size and thickness of accreted terranes (Wells et al., 1998; Egbert et al., 2022) and subaccreted sediments (Delph et al., 2021), may also contribute to the observed lateral variations in H_c. Furthermore, trench-normal variations in the elastic contrast of the overriding plate (Luo HP and Wang KL, 2021; McKenzie et al., 2022; D'Acquisto et al., 2023) and the viscosity contrast in the mantle wedge (Li SY et al., 2018a) may influence the lateral estimation of H_c.

Despite these influencing factors, lateral variations in H_c have been neglected in previous viscoelastic models of Cascadia (e.g., Wang KL et al., 2012; Li SY et al., 2018b). Given the widespread lateral variation in oceanic plate age across accretionary subduction zones, lateral heterogeneity in H_c is likely common. Incorporating such variations into earthquake-cycle deformation models (e.g., interseismic and postseismic models) could significantly alter predictions of horizontal and vertical deformation, owing to the effect of the D/H_c ratio on surface deformation patterns (Li SY and Chen L, 2023, 2024a). Because of the trade-off between H_c and D, refining H_c in 3D models will also enhance the precision of D estimates, thereby improving seismic hazard assessments (e.g., Ramos et al., 2021; Chan et al., 2023) and advancing our understanding of fault mechanics in conjunction with other geophysical observations (e.g., Carbotte et al., 2024; Fisher and Hirth, 2024).

Our results show that H_c carries greater uncertainty in its estimation compared with D (horizontal error bars in Figure 8), suggesting that H_c is a parameter more difficult to constrain. In contrast, D values remain relatively consistent around ~10 km depth along the margin (Figure 8b), consistent with previous studies that have obtained laterally uniform locking based on geodetic and thermal models (Hyndman and Wang K, 1995; Wang KL et al., 2003). The

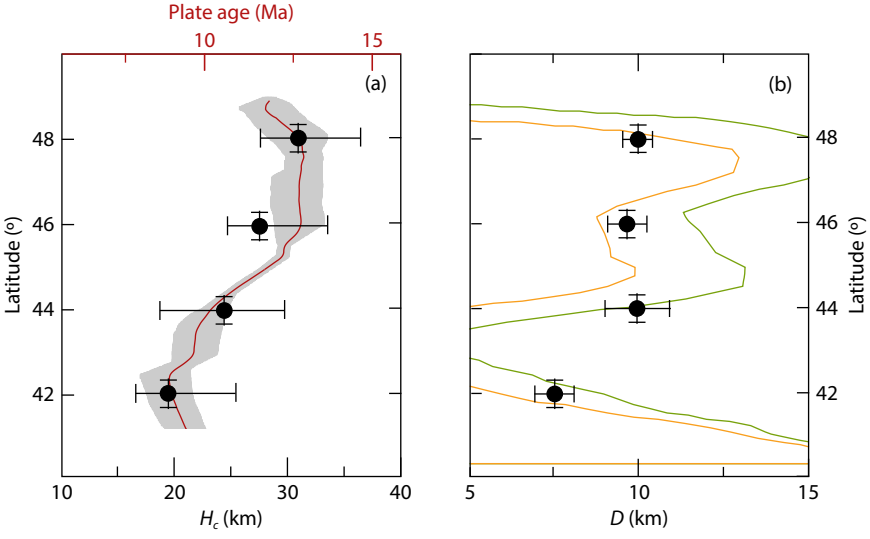

Figure 8. Lateral variations of the preferred (a) H_c and (b) D (black dots with error bars) based on multiple constraints. In (a), the red curve with gray shading is the plate age beneath the forearc from Wilson (2002), processed by Bodmer et al. (2020). In (b), the orange and green curves represent the preferred 0.8 and 0.7 locking degree distributions, respectively, from Li SY et al. (2018b), derived using a 3D viscoelastic model with a uniform 40-km upper-plate elastic thickness. Vertical error bars represent the width of the data profile (80 km), and horizontal error bars are obtained from modeling.

trend of slightly deeper locking depths in the north compared with the south also aligns with results from the 3D viscoelastic locking model of Li SY et al. (2018b; Figure 8b), supporting the robustness of our 2D approach for constraining both H_c and D.

4. Further Discussion

Our findings of H_c and D may have implications for understanding faulting processes and the physics of ETS, which commonly invoked low normal stress and elevated pore-fluid pressure along a narrowed fault zone of the plate interface at ETS depths (e.g., Liu YJ and Rice, 2007; Peacock, 2009; Audet and Bürgmann, 2014; Gao X and Wang KL, 2017; Bürgmann, 2018; Im et al., 2020; Behr and Bürgmann, 2021; Ando et al., 2023; Perfettini and Molinari, 2023). Compared with Nankai, where ETS typically occurs at 30–40 km depth, ETS events in Cascadia also occur at similar depths but under thermal conditions approximately 100 °C higher. This difference suggests that the thermal structure or metamorphic reactions may not be the primary controlling factors at different margins (Peacock, 2009; Syracuse et al., 2010). Given the lateral variability in H_c (Figure 8a) and its much shallower depth than that of the ETS zone, ETS may also not be directly or strongly governed by lithosphere–asthenosphere rheological layering—such as the H_c variations observed here—but instead by depth-dependent mechanical processes (e.g., stress or pore-fluid pressure conditions, or both), which warrant further investigation.

Our 2D models reveal pronounced along-strike variation in H_c (Figure 8a), underscoring the importance of 3D effects in the Cascadia Subduction Zone. By assuming uniformity out-of-plane, 2D sections systematically underestimate the locking depth, D, and—because of the trade-off between D and H_c (Figure 6)—likewise bias H_c toward lower and less variable values. A fully 3D treatment would therefore likely yield even greater along-strike contrasts in H_c. However, inversions of the 3D viscoelastic structure remain technically and computationally challenging: each forward simulation requires structure refinement to capture lateral heterogeneity, and the inversion must navigate a substantially larger parameter space. Moreover, the regularization inherent in most inverse methods tends to smooth true variations in both H_c and D. Addressing these 3D challenges will require advances in both numerical techniques and inversion strategies. Although a handful of studies have embedded seismologically or gravity-inferred 3D crust–mantle structures into crustal deformation models (e.g., Moreno et al., 2009), robust geodetic constraints on along-strike variations of H_c are still lacking for most convergent margins.

To our knowledge, this is the first study to deliberately constrain the lateral variation of H_c by exploiting interseismic surface deformation induced by megathrust locking and its ensuing viscoelastic mantle relaxation (Li SY et al., 2020). Future work involving additional case studies will enable meaningful global comparisons; however, this endeavor hinges on either properly correcting for postseismic effects in the geodetic data or focusing on margins that are unequivocally in the interseismic phase of the seismic cycle (Li SY and Chen L, 2023). We here propose that subaccretion-driven tectonics and accretionary-wedge cooling in Cascadia underpin the apparent correlation between H_c and the age of the subducting plate—a relationship that may not persist in margins characterized by different tectonic regimes. For example, although no investigation has yet linked lateral variation of H_c to short-term interseismic deformation in the Nankai margin, the long-term elastic thickness of its upper-plate lithosphere inferred from topography and gravity data is relatively uniform (~30 km; Kudo et al., 2001) and correlates with the along-strike variation in ETS depth. A globally self-consistent synthesis of H_c and D studies with interseismic deformation will ultimately shed light on the common processes operating across diverse convergent margins throughout the earthquake cycle.

5. Conclusions

Our 2D forward viscoelastic earthquake-cycle modeling of interseismic GNSS data across Cascadia reveals a significant trade-off between elastic upper-plate thickness (H_c) and locking depth (D), emphasizing the need to jointly consider multiple data types and geophysical constraints to robustly resolve both parameters. Whereas D remains relatively consistent (~10 km) along strike, H_c exhibits a systematic northward increase that correlates with oceanic plate age, suggesting a tectonic control likely linked to subaccretionary processes and accretionary wedge growth. This lateral variation in H_c, often neglected in previous earthquake-cycle deformation models, has important implications for interpreting interseismic and postseismic surface deformation, refining seismic hazard assessments, and understanding the mechanics of ETS. Our findings underscore the importance of accounting for trench-parallel heterogeneities in future 3D viscoelastic modeling efforts to compare with different margins and better capture the complexity of subduction zone dynamics.

Acknowledgments

All the data used in this work were previously published and can be accessed. We thank JianFeng Yang and the colleagues at COFFICE 422 in the Institute of Geology and Geophysics, Chinese Academy of Sciences, for stimulating discussions. Most figures in this paper were generated with the Generic Mapping Tools software (Wessel and Smith, 1998), and some were plotted with perceptually uniform color maps (Crameri, 2018). This work was supported by the National Key R&D Program of China (Grant No. 2023YFF0803200) and the National Natural Science Foundation of China (Grant No. 42288201).

References

Aagaard, B. T., Knepley, M. G., and Williams, C. A. (2013). A domain decomposition approach to implementing fault slip in finite-element models of quasi-static and dynamic crustal deformation. *J. Geophys. Res.: Solid Earth*, *118*(6), 3059–3079. https://doi.org/10.1002/jgrb.50217

Ando, R., Ujiie, K., Nishiyama, N., and Mori, Y. (2023). Depth-dependent slow earthquakes controlled by temperature dependence of brittle-ductile transitional rheology. *Geophys. Res. Lett.*, *50*(5), e2022GL101388. https://doi.org/10.1029/2022GL101388

Atwater, B. F. (1987). Evidence for great Holocene earthquakes along the outer coast of Washington State. *Science*, *236*(4804), 942–944. https://doi.org/10.1126/science.236.4804.942

Audet, P., and Bürgmann, R. (2014). Possible control of subduction zone slow-earthquake periodicity by silica enrichment. *Nature*, *510*(7505), 389–392. https://doi.org/10.1038/nature13391

Audet, P., and Kim, Y. (2016). Teleseismic constraints on the geological environment of deep episodic slow earthquakes in subduction zone

forearcs: A review. *Tectonophysics*, *670*, 1–15. https://doi.org/10.1016/j.tecto.2016.01.005

Behr, W. M., and Bürgmann, R. (2021). What's down there? The structures, materials and environment of deep-seated slow slip and tremor. *Philos. Trans. Roy. Soc. A: Math. Phys. Eng. Sci.*, *379*(2193), 20200218. https://doi.org/10.1098/rsta.2020.0218

Bilham, R., Mencin, D., Bendick, R., and Bürgmann, R. (2017). Implications for elastic energy storage in the Himalaya from the Gorkha 2015 earthquake and other incomplete ruptures of the Main Himalayan Thrust. *Quat. Int.*, *462*, 3–21. https://doi.org/10.1016/j.quaint.2016.09.055

Blakely, R. J., Brocher, T. M., and Wells, R. E. (2005). Subduction-zone magnetic anomalies and implications for hydrated forearc mantle. *Geology*, *33*(6), 445–448. https://doi.org/10.1130/G21447.1

Bodmer, M., Toomey, D. R., Roering, J. J., and Karlstrom, L. (2020). Asthenospheric buoyancy and the origin of high-relief topography along the Cascadia forearc. *Earth Planet. Sci. Lett.*, *531*, 115965. https://doi.org/10.1016/j.epsl.2019.115965

Bott, M. H. P., and Dean, D. S. (1973). Stress diffusion from plate boundaries. *Nature*, *243*(5406), 339–341. https://doi.org/10.1038/243339a0

Bürgmann, R., and Dresen, G. (2008). Rheology of the lower crust and upper mantle: Evidence from rock mechanics, geodesy, and field observations. *Annu. Rev. Earth Planet. Sci.*, *36*, 531–567. https://doi.org/10.1146/annurev.earth.36.031207.124326

Bürgmann, R. (2018). The geophysics, geology and mechanics of slow fault slip. *Earth Planet. Sci. Lett.*, *495*, 112–134. https://doi.org/10.1016/j.epsl.2018.04.062

Burov, E. B. (2011). Rheology and strength of the lithosphere. *Mar. Pet. Geol.*, *28*(8), 1402–1443. https://doi.org/10.1016/j.marpetgeo.2011.05.008

Cao, Z. B., and Liu, L. J. (2024). Western US intraplate deformation controlled by the complex lithospheric structure. *Nat. Commun.*, *15*(1), 3917. https://doi.org/10.1038/s41467-024-48223-2

Carbotte, S. M., Boston, B., Han, S. S., Shuck, B., Beeson, J., Canales, J. P., Tobin, H., Miller, N., Nedimovic, M., … Gahlawat, R. (2024). Subducting plate structure and megathrust morphology from deep seismic imaging linked to earthquake rupture segmentation at Cascadia. *Sci. Adv.*, *10*(23), eadl3198. https://doi.org/10.1126/sciadv.adl3198

Chan, Y. P. B., Yao, S. L., and Yang, H. F. (2023). Impact of hypocenter location on rupture extent and ground motion: A case study of Southern Cascadia. *J. Geophys. Res.: Solid Earth*, *128*(8), e2023JB026371. https://doi.org/10.1029/2023JB026371

Chen, L., Zheng, T. Y., and Xu, W. W. (2006). A thinned lithospheric image of the Tanlu Fault Zone, eastern China: Constructed from wave equation based receiver function migration. *J. Geophys. Res.: Solid Earth*, *111*(B9), B09312. https://doi.org/10.1029/2005JB003974

Chen, W. P., and Molnar, P. (1983). Focal depths of intracontinental and intraplate earthquakes and their implications for the thermal and mechanical properties of the lithosphere. *J. Geophys. Res.: Solid Earth*, *88*(B5), 4183–4214. https://doi.org/10.1029/JB088iB05p04183

Cohen, S. C. (1999). Numerical models of crustal deformation in seismic zones. *Adv. Geophys.*, *41*, 133–231. https://doi.org/10.1016/S0065-2687(08)60027-8

Crameri, F. (2018). Geodynamic diagnostics, scientific visualisation and StagLab 3.0. *Geoscientific Model Development, 11*(6), 2541–2562. https://doi.org/10.5194/gmd-11-2541-2018

D'Acquisto, M., Broerse, T., Marsman, C. P., and Govers, R. (2023). Reconciling the conflicting extent of overriding plate deformation before and during megathrust earthquakes in South America, Sunda and northeast Japan. *Geophys. J. Int.*, *235*(1), 879–908. https://doi.org/10.1093/gji/ggad262

Delph, J. R., Thomas, A. M., and Levander, A. (2021). Subcretionary tectonics: Linking variability in the expression of subduction along the Cascadia forearc. *Earth Planet. Sci. Lett.*, *556*, 116724. https://doi.org/10.1016/j.epsl.2020.116724

DeMets, C., Gordon, R. G., and Argus, D. F. (2010). Geologically current plate motions. *Geophys. J. Int.*, *181*(1), 1–80. https://doi.org/10.1111/j.1365-246X.2009.04491.x

Diao, F. Q., Wang, R. J., Zhu, Y. G., and Xiong, X. (2022). Revisiting the fault locking of the central Himalayan thrust with a viscoelastic earthquake-cycle deformation model. *Seismol. Res. Lett.*, *93*(1), 193–200. https://doi.org/10.1785/0220200310

Dragert, H., Wang, K. L., and James, T. S. (2001). A silent slip event on the deeper Cascadia subduction interface. *Science*, *292*(5521), 1525–1528. https://doi.org/10.1126/science.1060152

Egbert, G. D., Yang, B., Bedrosian, P. A., Key, K., Livelybrooks, D. W., Schultz, A., Kelbert, A., and Parris, B. (2022). Fluid transport and storage in the Cascadia forearc influenced by overriding plate lithology. *Nat. Geosci.*, *15*(8), 677–682. https://doi.org/10.1038/s41561-022-00981-8

Epstein, G. S., Condit, C. B., Stoner, R. K., Holt, A. F., and Guevara, V. E. (2024). Evolving subduction zone thermal structure drives extensive forearc mantle wedge hydration. *AGU Adv.*, *5*(4), e2023AV001121. https://doi.org/10.1029/2023AV001121

Fischer, K. M., Ford, H. A., Abt, D. L., and Rychert, C. A. (2010). The lithosphere-asthenosphere boundary. *Annu. Rev. Earth Planet. Sci.*, *38*, 551–575. https://doi.org/10.1146/annurev-earth-040809-152438

Fisher, D. M., and Hirth, G. (2024). A pressure solution flow law for the seismogenic zone: Application to Cascadia. *Sci. Adv.*, *10*(4), eadi7279. https://doi.org/10.1126/sciadv.adi7279

Freed, A. M., Hashima, A., Becker, T. W., Okaya, D. A., Sato, H., and Hatanaka, Y. (2017). Resolving depth-dependent subduction zone viscosity and afterslip from postseismic displacements following the 2011 Tohoku-oki, Japan earthquake. *Earth Planet. Sci. Lett.*, *459*, 279–290. https://doi.org/10.1016/j.epsl.2016.11.040

Fukuda, J., and Johnson, K. M. (2021). Bayesian inversion for a stress-driven model of afterslip and viscoelastic relaxation: Method and application to postseismic deformation following the 2011 M_w 9.0 Tohoku-Oki earthquake. *J. Geophys. Res.: Solid Earth*, *126*(5), e2020JB021620. https://doi.org/10.1029/2020JB021620

Gao, D. W., Wang, K. L., Davis, E. E., Jiang, Y., Insua, T. L., and He, J. H. (2017). Thermal state of the Explorer segment of the Cascadia subduction zone: Implications for seismic and tsunami hazards. *Geochem., Geophys., Geosyst.*, *18*(4), 1569–1579. https://doi.org/10.1002/2017GC006838

Gao, X., and Wang, K. L. (2017). Rheological separation of the megathrust seismogenic zone and episodic tremor and slip. *Nature*, *543*(7645), 416–419. https://doi.org/10.1038/nature21389

Goldfinger, C., Galer, S., Beeson, J., Hamilton, T., Black, B., Romsos, C., Patton, J., Nelson, C. H., Hausmann, R., and Morey, A. (2017). The importance of site selection, sediment supply, and hydrodynamics: A case study of submarine paleoseismology on the Northern Cascadia margin, Washington USA. *Mar. Geol.*, *384*, 4–16, 17, 25–46. https://doi.org/10.1016/j.margeo.2016.06.008

Hetland, E. A., and Hager, B. H. (2006). Interseismic strain accumulation: Spin-up, cycle invariance, and irregular rupture sequences. *Geochem., Geophys., Geosyst.*, *7*(5), Q05004. https://doi.org/10.1029/2005GC001087

Hirth, G., and Kohlstedt, D. (2004). Rheology of the upper mantle and the mantle wedge: A view from the experimentalists. In J. Eiler (Ed.), *Inside the Subduction Factory* (pp. 83–106). Washington, DC: American Geophysical Union. https://doi.org/10.1029/138GM06

Hu, Y., Bürgmann, R., Banerjee, P., Feng, L. J., Hill, E. M., Ito, T., Tabei, T., and Wang, K. L. (2016). Asthenosphere rheology inferred from observations of the 2012 Indian Ocean earthquake. *Nature*, *538*(7625), 368–372. https://doi.org/10.1038/nature19787

Hyndman, R. D., and Wang, K. (1995). The rupture zone of Cascadia great earthquakes from current deformation and the thermal regime. *J. Geophys. Res.: Solid Earth*, *100*(B11), 22133–22154. https://doi.org/10.1029/95JB01970

Hyndman, R. D., Yamano, M., and Oleskevich, D. A. (1997). The seismogenic zone of subduction thrust faults. *Island Arc*, *6*(3), 244–260. https://doi.org/10.1111/j.1440-1738.1997.tb00175.x

Hyndman, R. D. (2013). Downdip landward limit of Cascadia great earthquake rupture. *J. Geophys. Res.: Solid Earth*, *118*(10), 5530–5549. https://doi.org/10.1002/jgrb.50390

Im, K., Saffer, D., Marone, C., and Avouac, J. P. (2020). Slip-rate-dependent friction as a universal mechanism for slow slip events. *Nat. Geosci.*, *13*(10), 705–710. https://doi.org/10.1038/s41561-020-0627-9

Itoh, Y., Wang, K. L., Nishimura, T., and He, J. H. (2019). Compliant volcanic arc and backarc crust in Southern Kurile suggested by interseismic geodetic

deformation. *Geophys. Res. Lett.*, *46*(21), 11790–11798. https://doi.org/10.1029/2019GL084656

Kawakatsu, H., Kumar, P., Takei, Y., Shinohara, M., Kanazawa, T., Araki, E., and Suyehiro, K. (2009). Seismic evidence for sharp lithosphere-asthenosphere boundaries of oceanic plates. *Science*, *324*(5926), 499–502. https://doi.org/10.1126/science.1169499

Khazaradze, G., Qamar, A., and Dragert, H. (1999). Tectonic deformation in western Washington from continuous GPS measurements. *Geophys. Res. Lett.*, *26*(20), 3153–3156. https://doi.org/10.1029/1999GL010458

Kudo, T., Yamaji, A., Furumoto, M., and Nagao, T. (2001). Effective elastic thickness of island arc lithosphere under Japan. *Island Arc*, *10*(2), 135–144. https://doi.org/10.1111/j.1440-1738.2001.00314.x

Li, S. Y., Moreno, M., Bedford, J., Rosenau, M., and Oncken, O. (2015). Revisiting viscoelastic effects on interseismic deformation and locking degree: A case study of the Peru-North Chile subduction zone. *J. Geophys. Res.: Solid Earth*, *120*(6), 4522–4538. https://doi.org/10.1002/2015JB011903

Li, S. Y., Bedford, J., Moreno, M., Barnhart, W. D., Rosenau, M., and Oncken, O. (2018a). Spatiotemporal variation of mantle viscosity and the presence of cratonic mantle inferred from 8 years of postseismic deformation following the 2010 Maule, Chile, earthquake. *Geochem., Geophys., Geosyst.*, *19*(9), 3272–3285. https://doi.org/10.1029/2018GC007645

Li, S. Y., Wang, K. L., Wang, Y. Z., Jiang, Y., and Dosso, S. E. (2018b). Geodetically inferred locking state of the Cascadia megathrust based on a viscoelastic Earth model. *J. Geophys. Res.: Solid Earth*, *123*(9), 8056–8072. https://doi.org/10.1029/2018JB015620

Li, S. Y., Fukuda, J., and Oncken, O. (2020). Geodetic evidence of time-dependent viscoelastic interseismic deformation driven by megathrust locking in the southwest Japan subduction zone. *Geophys. Res. Lett.*, *47*(4), e2019GL085551. https://doi.org/10.1029/2019GL085551

Li, S. Y., and Chen, L. (2022). Elastic slab in viscoelastic mantle: Effects on determining megathrust slip and mantle viscosity during postseismic and interseismic phases. *J. Geophys. Res.: Solid Earth*, *127*(8), e2022JB024730. https://doi.org/10.1029/2022JB024730

Li, S. Y., and Chen, L. (2023). How long can the postseismic and interseismic phases of great subduction earthquake sustain? Toward an integrated earthquake-cycle perspective. *Geophys. Res. Lett.*, *50*(11), e2023GL103976. https://doi.org/10.1029/2023GL103976

Li, S. Y., and Chen, L. (2024a). Vertical crustal deformation due to viscoelastic earthquake cycles at subduction zones: Implications for Nankai and Cascadia. *J. Geophys. Res.: Solid Earth*, *129*(8), e2024JB028817. https://doi.org/10.1029/2024JB028817

Li, S. Y., and Chen, L. (2024b). Revisiting interseismic deformation in Nankai: Focusing on slip-deficit accumulation in the ETS zone and comparison with Cascadia. *Earth, Planets Space*, *76*(1), 108. https://doi.org/10.1186/s40623-024-02054-z

Littel, G. F., Thomas, A. M., and Baltay, A. S. (2018). Using tectonic tremor to constrain seismic wave attenuation in Cascadia. *Geophys. Res. Lett.*, *45*(18), 9579–9587. https://doi.org/10.1029/2018GL079344

Liu, Y. J., and Rice, J. R. (2007). Spontaneous and triggered aseismic deformation transients in a subduction fault model. *J. Geophys. Res.: Solid Earth*, *112*(B9), B09404. https://doi.org/10.1029/2007JB004930

Lu, G., Zhao, L., Chen, L., Wan, B. and Wu, F. Y. (2021). Reviewing subduction initiation and the origin of plate tectonics: What do we learn from present-day Earth?. *Earth Planet. Phys.*, *5*(2), 123–140. https://doi.org/10.26464/epp2021014

Luo, H. P., and Wang, K. L. (2021). Postseismic geodetic signature of cold forearc mantle in subduction zones. *Nat. Geosci.*, *14*(2), 104–109. https://doi.org/10.1038/s41561-020-00679-9

McCaffrey, R. (2002). Crustal block rotations and plate coupling. In S. Stein, et al. (Eds.), *Plate Boundary Zones* (pp. 101–122). Washington, DC: American Geophysical Union. https://doi.org/10.1029/GD030p0101

McCaffrey, R., King, R. W., Payne, S. J., and Lancaster, M. (2013). Active tectonics of northwestern U. S. inferred from GPS-derived surface velocities. *J. Geophys. Res.: Solid Earth*, *118*(2), 709–723. https://doi.org/10.1029/2012JB009473

McCrory, P. A., Blair, J. L., Waldhauser, F., and Oppenheimer, D. H. (2012). Juan de Fuca slab geometry and its relation to Wadati-Benioff zone seismicity. *J. Geophys. Res.: Solid Earth*, *117*(B9), B09306. https://doi.org/10.1029/2012JB009407

McKenzie, D. P. (1967). Some remarks on heat flow and gravity anomalies. *J. Geophys. Res.*, *72*(24), 6261–6273. https://doi.org/10.1029/JZ072i024p06261

McKenzie, K. A., Furlong, K. P., and Herman, M. W. (2022). Regional and local patterns of upper-plate deformation in Cascadia: The importance of the down-dip extent of locking relative to upper-plate strength contrasts. *Tectonics*, *41*(1), e2021TC007062. https://doi.org/10.1029/2021TC007062

Meade, B. J., and Loveless, J. P. (2009). Block modeling with connected fault-network geometries and a linear elastic coupling estimator in spherical coordinates. *Bull. Seismol. Soc. Am.*, *99*(6), 3124–3139. https://doi.org/10.1785/0120090088

Michel, S., Gualandi, A., and Avouac, J. P. (2019). Interseismic coupling and slow slip events on the Cascadia megathrust. *Pure Appl. Geophys.*, *176*(9), 3867–3891. https://doi.org/10.1007/s00024-018-1991-x

Moreno, M. S., Bolte, J., Klotz, J., and Melnick, D. (2009). Impact of megathrust geometry on inversion of coseismic slip from geodetic data: Application to the 1960 Chile earthquake. *Geophys. Res. Lett.*, *36*(16), L16310. https://doi.org/10.1029/2009GL039276

Muto, J., Shibazaki, B., Iinuma, T., Ito, Y., Ohta, Y., Miura, S., and Nakai, Y. (2016). Heterogeneous rheology controlled postseismic deformation of the 2011 Tohoku-Oki earthquake. *Geophys. Res. Lett.*, *43*(10), 4971–4978. https://doi.org/10.1002/2016GL068113

Muto, J., Moore, J. D. P., Barbot, S., Iinuma, T., Ohta, Y., and Iwamori, H. (2019). Coupled afterslip and transient mantle flow after the 2011 Tohoku earthquake. *Sci. Adv.*, *5*(9), eaaw1164. https://doi.org/10.1126/sciadv.aaw1164

Noda, A., Saito, T., and Fukuyama, E. (2018). Slip-deficit rate distribution along the Nankai Trough, southwest Japan, with elastic lithosphere and viscoelastic asthenosphere. *J. Geophys. Res.: Solid Earth*, *123*(9), 8125–8142. https://doi.org/10.1029/2018JB015515

Nur, A., and Mavko, G. (1974). Postseismic viscoelastic rebound. *Science*, *183*(4121), 204–206. https://doi.org/10.1126/science.183.4121.204

Obara, K. (2002). Nonvolcanic deep tremor associated with subduction in southwest Japan. *Science*, *296*(5573), 1679–1681. https://doi.org/10.1126/science.1070378

Okada, Y. (1992). Internal deformation due to shear and tensile faults in a half-space. *Bull. Seismol. Soc. Am.*, *82*(2), 1018–1040. https://doi.org/10.1785/BSSA0820021018

Oleskevich, D. A., Hyndman, R. D., and Wang, K. (1999). The updip and downdip limits to great subduction earthquakes: Thermal and structural models of Cascadia, south Alaska, SW Japan, and Chile. *J. Geophys. Res.: Solid Earth*, *104*(B7), 14965–14991. https://doi.org/10.1029/1999JB900060

Peacock, S. M. (2009). Thermal and metamorphic environment of subduction zone episodic tremor and slip. *J. Geophys. Res.: Solid Earth*, *114*(B8), B00A07. https://doi.org/10.1029/2008JB005978

Peltier, W. R., Argus, D. F., and Drummond, R. (2015). Space geodesy constrains ice age terminal deglaciation: The global ICE-6G_C (VM5a) model. *J. Geophys. Res.: Solid Earth*, *120*(1), 450–487. https://doi.org/10.1002/2014JB011176

Perfettini, H., and Molinari, A. (2023). The interaction between frictional slip and viscous fault root produces slow slip events. *J. Geophys. Res.: Solid Earth*, *128*(3), e2022JB024645. https://doi.org/10.1029/2022JB024645

Pollitz, F., Banerjee, P., Grijalva, K., Nagarajan, B., and Bürgmann, R. (2008). Effect of 3-D viscoelastic structure on post-seismic relaxation from the 2004 M = 9.2 Sumatra earthquake. *Geophys. J. Int.*, *173*(1), 189–204. https://doi.org/10.1111/j.1365-246X.2007.03666.x

Pollitz, F. F., and Evans, E. L. (2017). Implications of the earthquake cycle for inferring fault locking on the Cascadia megathrust. *Geophys. J. Int.*, *209*(1), 167–185. https://doi.org/10.1093/gji/ggx009

Pollitz, F. F. (2025). 3D viscoelastic models of slip-deficit rate along the Cascadia subduction zone. *J. Geophys. Res.: Solid Earth*, *130*(1), e2024JB029847. https://doi.org/10.1029/2024JB029847

Porritt, R. W., Allen, R. M., Boyarko, D. C., and Brudzinski, M. R. (2011). Investigation of Cascadia segmentation with ambient noise tomography. *Earth Planet. Sci. Lett.*, *309*(1-2), 67–76. https://doi.org/10.1016/j.epsl.2011.06.026

Qiu, Q., Moore, J. D. P., Barbot, S., Feng, L. J., and Hill, E. M. (2018). Transient rheology of the Sumatran mantle wedge revealed by a decade of great earthquakes. *Nat. Commun.*, *9*(1), 995. https://doi.org/10.1038/s41467-018-03298-6

Ramos, M. D., Huang, Y. H., Ulrich, T., Li, D., Gabriel, A. A., and Thomas, A. M. (2021). Assessing margin-wide rupture behaviors along the Cascadia megathrust with 3-D dynamic rupture simulations. *J. Geophys. Res.: Solid Earth*, *126*(7), e2021JB022005. https://doi.org/10.1029/2021JB022005

Rogers, G., and Dragert, H. (2003). Episodic tremor and slip on the Cascadia subduction zone: The chatter of silent slip. *Science*, *300*(5627), 1942–1943. https://doi.org/10.1126/science.1084783

Rychert, C. A., Harmon, N., Constable, S., and Wang, S. G. (2020). The nature of the lithosphere-asthenosphere boundary. *J. Geophys. Res.: Solid Earth*, *125*(10), e2018JB016463. https://doi.org/10.1029/2018JB016463

Satake, K., Wang, K. L., and Atwater, B. F. (2003). Fault slip and seismic moment of the 1700 Cascadia earthquake inferred from Japanese tsunami descriptions. *J. Geophys. Res.: Solid Earth*, *108*(B11), 2535. https://doi.org/10.1029/2003JB002521

Sato, D. S., Hori, T., and Fukahata, Y. (2024). Differentiating frictionally locked asperities from kinematically coupled zones. *arXiv preprint arXiv*: 2409.14266. https://doi.org/10.48550/arXiv.2409.14266

Savage, J. C. (1983). A dislocation model of strain accumulation and release at a subduction zone. *J. Geophys. Res.: Solid Earth*, *88*(B6), 4984–4996. https://doi.org/10.1029/JB088iB06p04984

Schmalzle, G. M., McCaffrey, R., and Creager, K. C. (2014). Central Cascadia subduction zone creep. *Geochem., Geophys., Geosyst.*, *15*(4), 1515–1532. https://doi.org/10.1002/2013GC005172

Shelly, D. R., Beroza, G. C., and Ide, S. (2007). Non-volcanic tremor and low-frequency earthquake swarms. *Nature*, *446*(7133), 305–307. https://doi.org/10.1038/nature05666

Sherrill, E. M., Johnson, K. M., and Jackson, N. M. (2024). Locating boundaries between locked and creeping regions at Nankai and Cascadia subduction zones. *J. Geophys. Res.: Solid Earth*, *129*(10), e2024JB029346. https://doi.org/10.1029/2024JB029346

Sobolev, S. V., and Muldashev, I. A. (2017). Modeling seismic cycles of great megathrust earthquakes across the scales with focus at postseismic phase. *Geochem., Geophys., Geosyst.*, *18*(12), 4387–4408. https://doi.org/10.1002/2017GC007230

Suito, H., and Freymueller, J. T. (2009). A viscoelastic and afterslip postseismic deformation model for the 1964 Alaska earthquake. *J. Geophys. Res.: Solid Earth*, *114*(B11), B11404. https://doi.org/10.1029/2008JB005954

Sun, T. H. Z., Wang, K. L., Iinuma, T., Hino, R., He, J. H., Fujimoto, H., Kido, M., Osada, Y., Miura, S., … Hu, Y. (2014). Prevalence of viscoelastic relaxation after the 2011 Tohoku-oki earthquake. *Nature*, *514*(7520), 84–87. https://doi.org/10.1038/nature13778

Syracuse, E. M., van Keken, P. E., and Abers, G. A. (2010). The global range of subduction zone thermal models. *Phys. Earth Planet. Inter.*, *183*(1-2), 73–90. https://doi.org/10.1016/j.pepi.2010.02.004

Toda, S., and Stein, R. S. (2022). Central shutdown and surrounding activation of aftershocks from megathrust earthquake stress transfer. *Nat. Geosci.*, *15*(6), 494–500. https://doi.org/10.1038/s41561-022-00954-x

Trubienko, O., Fleitout, L., Garaud, J. D., and Vigny, C. (2013). Interpretation of interseismic deformations and the seismic cycle associated with large subduction earthquakes. *Tectonophysics*, *589*, 126–141. https://doi.org/10.1016/j.tecto.2012.12.027

Wang, K. L., He, J. H., Dragert, H., and James, T. S. (2001). Three-dimensional viscoelastic interseismic deformation model for the Cascadia subduction zone. *Earth, Planets Space, 53*(4), 295–306. https://doi.org/10.1186/BF03352386

Wang, K. L., Wells, R., Mazzotti, S., Hyndman, R. D., and Sagiya, T. (2003). A revised dislocation model of interseismic deformation of the Cascadia subduction zone. *J. Geophys. Res.: Solid Earth*, *108*(B1), 2026. https://doi.org/10.1029/2001JB001227

Wang, K. L., Hu, Y., and He, J. H. (2012). Deformation cycles of subduction earthquakes in a viscoelastic Earth. *Nature*, *484*(7394), 327–332. https://doi.org/10.1038/nature11032

Wang, K. L., and Tréhu, A. M. (2016). Invited review paper: Some outstanding issues in the study of great megathrust earthquakes—The Cascadia example. *J. Geodyn.*, *98*, 1–18. https://doi.org/10.1016/j.jog.2016.03.010

Wang, R. J., Lorenzo-Martín, F., and Roth, F. (2006). PSGRN/PSCMP—A new code for calculating co-and post-seismic deformation, geoid and gravity changes based on the viscoelastic-gravitational dislocation theory. *Comput. Geosci.*, *32*(4), 527–541. https://doi.org/10.1016/j.cageo.2005.08.006

Wang, X., Chen, L., Wang, K. L., Chen, Q. F., Zhan, Z. W., and Yang, J. F. (2024). Seismic evidence for melt-rich lithosphere-asthenosphere boundary beneath young slab at Cascadia. *Nat. Commun.*, *15*(1), 3504. https://doi.org/10.1038/s41467-024-47887-0

Weiss, J. R., Qiu, Q., Barbot, S., Wright, T. J., Foster, J. H., Saunders, A., Brooks, B. A., Bevis, M., Kendrick, E., … Echalar, A. (2019). Illuminating subduction zone rheological properties in the wake of a giant earthquake. *Sci. Adv.*, *5*(12), eaax6720. https://doi.org/10.1126/sciadv.aax6720

Wells, R. E., Weaver, C. S., and Blakely, R. J. (1998). Fore-arc migration in Cascadia and its neotectonic significance. *Geology*, *26*(8), 759–762. https://doi.org/10.1130/0091-7613(1998)026<0759:FAMICA>2.3.CO;2

Wessel, P., and Smith, W. H. (1998). New, improved version of Generic Mapping Tools released. *Eos, Transactions American Geophysical Union, 79*(47), 579–579. https://doi.org/10.1029/98eo00426

Wilson, D. S. (2002). The Juan de Fuca plate and slab-isochron structure and Cenozoic plate motions. *U.S. Geological Survey Open-File Report*, *02*(328), 9–12. https://doi.org/10.3133/ofr02328

Wirth, E. A., and Frankel, A. D. (2019). Impact of down-dip rupture limit and high-stress drop subevents on coseismic land-level change during Cascadia megathrust earthquakes. *Bull. Seismol. Soc. Am.*, *109*(6), 2187–2197. https://doi.org/10.1785/0120190043

Wiseman, K., Bürgmann, R., Freed, A. M., and Banerjee, P. (2015). Viscoelastic relaxation in a heterogeneous Earth following the 2004 Sumatra–Andaman earthquake. *Earth Planet. Sci. Lett.*, *431*, 308–317. https://doi.org/10.1016/j.epsl.2015.09.024

Yu, C. H., Xu, M., Kirby, J. F., Shi, X. B., and Jiménez-Díaz, A. (2022). Spatial variations of the effective elastic thickness and internal load fraction in the Cascadia subduction zone. *Geophys. J. Int.*, *229*(1), 487–504. https://doi.org/10.1093/gji/ggab495